Imaging Ultrafast Carrier Transport in Nanoscale Field-Effect Transistors

Byung Hee Son, Jae-Ku Park, Jung Taek Hong, Ji-Yong Park, Soonil Lee, and Yeong Hwan Ahn*

Department of Physics and Department of Energy Systems Research, Ajou University, Suwon 443-749, Korea

ABSTRACT In the present study, we visualize ultrafast carrier dynamics in one-dimensional nanoscale devices, such as Si nanowire and carbon nanotube transistors using femtosecond photocurrent microscopy. We investigate transit times of ultrashort carriers that are generated near one metallic electrode and subsequently transported toward the opposite electrode based on drift and diffusion motions. Conversely, pure diffusion motion is observed when the pump pulse is located in the middle of the nanowires. Carrier dynamics have been addressed for various working conditions, in which we found that the carrier velocity and pulse width can be manipulated by the external electrodes. In particular, the carrier velocities extracted from transit times increase for a larger negative gate bias because of the increased field strength at the Schottky barrier.

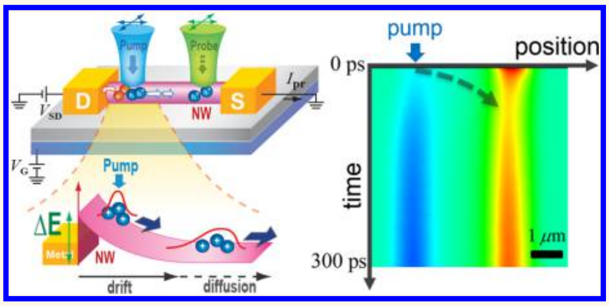

KEYWORDS: field-effect transistor · carrier transport · diffusion motion · nanowire · carbon nanotube · femtosecond

One-dimensional nanoscale devices, such as semiconductor nanowires (NWs) and single-walled carbon nanotubes (SWNTs), have been intensively investigated because of their potential application for future high-speed electronic, optoelectronic, and sensing devices.[1−6] Investigation of charge carrier dynamics with an ultrashort time scale is one of the primary steps necessary for developing high-speed electronic devices. The transit time of the charge carriers is the ultimate factor limiting the high-frequency response of nanoscale devices;[7] however, traditional radio frequency measurements are often limited by the high impedance or the RC constants of the devices.[8−12] Alternatively, optical ultrafast measurement techniques have been widely used to investigate charge carrier dynamics with a time resolution determined by the optical pulse width (down to a few femtoseconds).[13] Recently, researchers have reported visualizing charge carrier movements in free-standing Si NWs using an ultrafast pump−probe imaging technique.[14−16] The carrier diffusion motions induced by a pump pulse located in the middle of the NWs were visualized. In addition, transient absorption microscopy has been successfully introduced for studying the energy and the charge carrier movement in SWNTs, Au NWs, and monolayer WSe_2.[17−20] However, these optical measurements are limited for interrogating the carrier dynamics in operating devices fabricated on various substrates because they are frequently obscured by the substrate signals. Consequently, these techniques are not ideal for low-dimensional systems with NWs thinner than the optical spot size (<100 nm) or with SWNTs.

Scanning photocurrent microscopy (SPCM) techniques have been introduced as powerful tools for investigating local optoelectronic characteristics, such as metallic contacts, defects, interfaces, and junctions.[21−28] We were able to collect localized electronic band information that is not disturbed by signals originating from the substrate, and hence, compared with conventional optical techniques, SPCM can provide a higher signal-to-noise ratio. Only recently, ultrafast pump−probe photocurrent techniques have been demonstrated for studying carrier dynamics in SWNT devices by using collinear pump and probe beams.[29,30] In addition, ultrafast phenomena in graphene and GaAs NWs have been investigated by measuring terahertz radiation in specially designed circuit structures.[31,32] However, the carrier dynamics have not been directly visualized,

* Address correspondence to ahny@ajou.ac.kr.

Received for review July 31, 2014 and accepted October 22, 2014.

10.1021/nn5042619

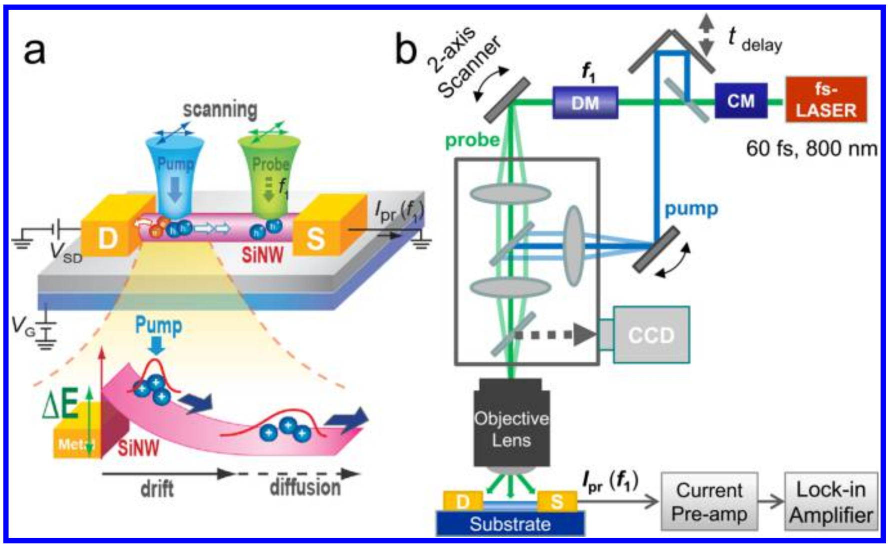

Figure 1. Schematic of experiments. (a) Schematic diagram of ultrafast carrier dynamics in a NW device. Photoinduced ultrafast carriers are generated by a femtosecond laser and then transported toward the other part of the NWs by drift and subsequent diffusion processes. (b) Schematic diagram of the experimental setup (CM, chirped mirrors; DM, deformable mirror).

in particular, with respect to various working conditions.

Here we present the first demonstration of femtosecond scanning photocurrent microscopy (fs-SPCM) on Si NWs and SWNT field-effect transistors (FETs). We generate ultrashort carriers at the FET channels by illuminating femtosecond laser pulses at Schottky contacts and monitor their subsequent migration toward different parts of NWs. We visualized their movements in terms of various working conditions such as source-drain and gate biases for NWs and SWNTs with various channel lengths. In addition, we introduce a possibility for ultrafast pulse shaping in which we control the time spread of the electrical pulse with the help of the external electrodes.

RESULTS AND DISCUSSION

As schematically presented in Figure 1a, ultrafast carrier dynamics in NW devices have been measured using a combination of scanning photocurrent microscopy[27,33,34] and time-resolved pump–probe techniques.[13] If we locate the femtosecond pump pulse near the metallic contacts (*i.e.*, the Schottky contacts with strong electronic band bending), an ultrashort carrier pulse will be generated and subsequently transported toward the middle of the NW by the drift motion resulting from built-in electric fields. Pure diffusion motions will follow once the carriers escape the depletion region. The carriers transported to the other part of the NWs can be monitored using the spatially separated probe pulses. This is because the carriers subjected to pump-induced migration will influence the photocurrent generated by the probe pulse (I_{pr}). The value of I_{pr} is recorded as a function of the position of both the pump and the probe pulses and also as a function of the time delay between them, enabling us to obtain a spatiotemporal image of carrier movements. The experimental setup is schematically shown in Figure 1b, and its detailed description is presented in the Methods section. Importantly, we monitor the probe photocurrent exclusively by using a lock-in technique. By comparison, the previous femtosecond photocurrent measurements on SWNTs record the two collinear pulses simultaneously and thus necessitate the nonlinear response of single-pulse excitation as a prerequisite condition.[30]

Figure 2a shows a typical photocurrent microscopic image of a Si NW device that has a channel length (l_{ch}) of 4 μm; this image is acquired by scanning the probe pulse (~60 fJ/pulse) in the absence of the pump pulse, with the voltages for both the source-drain bias (V_{SD}) and the gate bias (V_G) fixed at 0 V. Photocurrent spots near the metal contacts are clearly visible along the Si NWs. Both spots are located approximately 0.25 μm from their respective metal interfaces, and this configuration results in a relative distance of $d_{pc} \sim 3.5$ μm. In this figure, red (blue) indicates a positive (negative) current. The current spots near the metal electrodes originate from the electronic band bending at the electrode–NW interfaces, as reported in other studies.[21] Here, we are interested in visualizing the carrier movement created near one of the metallic contacts (denoted by S in Figure 2a) and the subsequent migration to the other side of the electrode (denoted by D), which is positioned 3.5 μm from the pump position.

In the presence of a pump pulse (~0.6 pJ/pulse), I_{pr} changes dramatically as a function of time delay (t_{delay}) for both the S and D signals. A series of I_{pr} images as a function of t_{delay} are provided in the Supporting Information S2. Here we demonstrate a two-dimensional plot of spatiotemporal imaging in Figure 2b, for a

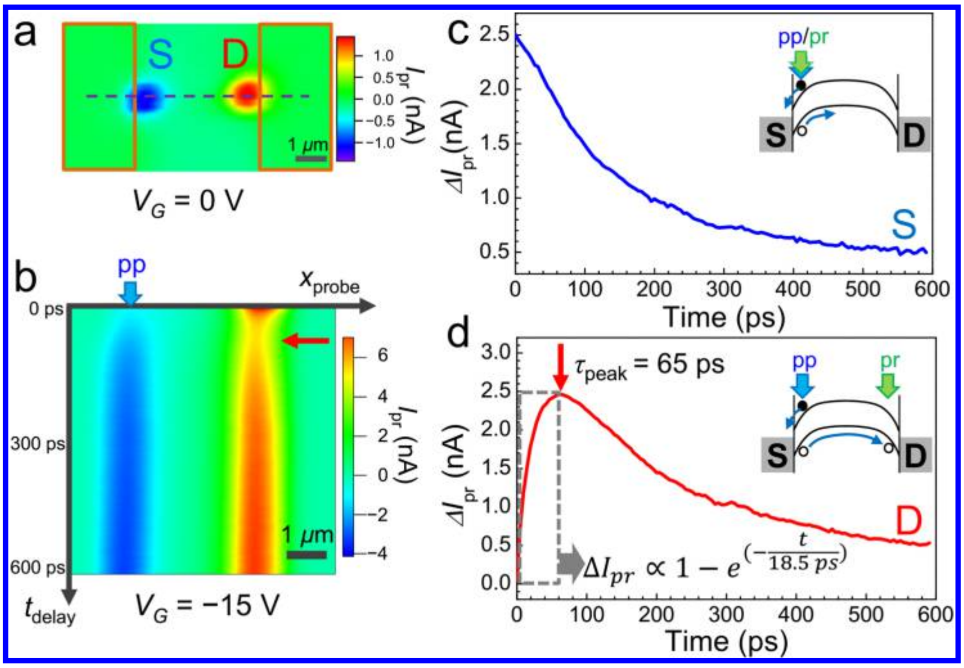

Figure 2. Spatiotemporal imaging of photogenerated carriers. (a) Typical photocurrent microscopy image of a Si NW device with I_{ch} = 4 μm without a pump pulse for $V_{SD} = V_G = 0$. (b) Plot of the spatiotemporal image obtained when the pump pulse is fixed at position S for $V_G = -15$ V. The *x*-axis represents the position along the dashed line in (a), and the *y*-axis represents time delay. The maximum change in signal I_{pr} at position D is denoted by a red arrow. (c) Time trace of ΔI_{pr} when the probe is positioned at S (when the probe spatially overlaps the pump pulse). ΔI_{pr} is defined as $|I_{pr} - I_{pr,off}|$, where $I_{pr,off}$ is the probe photocurrent without the pump pulse. (d) Time trace of ΔI_{pr} when the probe is positioned at D.

pump pulse at a fixed position (S). Specifically, we measure I_{pr} along the dashed line (X_{probe}) in Figure 2a while varying t_{delay} (0−600 ps). Both I_{pr} signals (at positions S and D) decrease noticeably in the presence of the pump pulse. In particular, I_{pr} is reduced significantly near the zero delay, which indicates that the change in I_{pr} primarily results from the presence of the pump pulse.

More importantly, when the probe pulse is positioned at D, the maximum change in I_{pr} is delayed, as indicated by a red arrow. The delayed change in I_{pr} at position D is caused by the migrated carriers (generated by the pump pulse), which are spatially separated at position S. When the electron and hole pairs are created in the band-bending region, the electrons move to the nearby metal electrode (S), while the holes are injected toward the opposite electrode (D) in p-type operation, as shown in the insets of Figure 2c,d. The migrated hole carriers occupy some of the states that would have been excited by the probe pulse, and this phenomenon results in the decreased I_{pr}. Alternatively, it is also plausible that the migrated carriers will influence the electronic band structures when the pump-induced carrier densities are large in high-intensity conditions. In our case, the maximum carrier density reaches $5 \times 10^{17}/\text{cm}^3$, right after the excitations, for the typical pulse energy of 0.6 pJ/pulse (we used an absorption coefficient of 1000 cm^{-1} for Si at 800 nm and a reflection loss of 32%). We would like to mention that the band alignment did not change noticeably at this density regime, which was confirmed by SPCM measurements conducted using the femtosecond lasers with the comparable intensity (see Supporting Information S5).

The magnitude of the change in I_{pr} (ΔI_{pr}) for positions S and D is plotted as a function of t_{delay} in Figure 2c,d, respectively. ΔI_{pr} is the absolute value of the change and thus yields the positive maximum value when I_{pr} is at the minimum in Figure 2b. For position S, ΔI_{pr} is largest at zero delay and gradually relaxes with a decay constant of 140 ps. The measurement of the carrier escape time for photogenerated carriers has been reported for SWNT devices by using the collinear pump−probe photocurrent technique.[30] Conversely, when we measure ΔI_{pr} on the opposite side of the electrode (at position D), ΔI_{pr} increases rapidly until it reaches its highest value at $\tau \sim 65$ ps. This transit time (τ_{peak}) corresponds to a carrier velocity of 5.4×10^6 cm/s. In addition, the initial increase in ΔI_{pr} for $t_{delay} < \tau_{peak}$ is well fitted by the relation $\Delta I_{pr} \propto 1 - \exp(-t_{delay}/\tau_c)$, where τ_c is the characteristic time constant (when ΔI_{pr} reaches 63% of its maximum value), which yields a value of 18.5 ps. Similar results on the different channel lengths are presented in the Supporting Information S3. We also note that carrier dynamics can be obtained for the probe pulse located in the middle of NWs, even though this visualization is not provided in Figure 2 because of the low contrast ratio relative to the metallic signals (Supporting Information S4). In addition, we found that the ΔI_{pr} increases

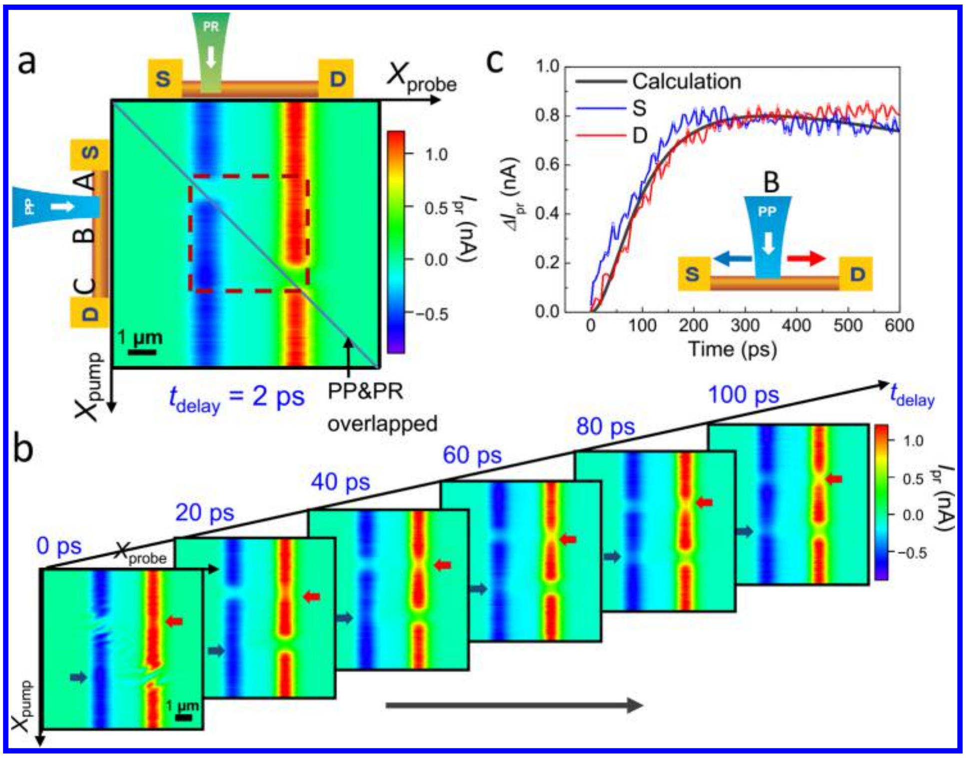

Figure 3. Pump−probe photocurrent correlation images. (a) Probe photocurrents are mapped as a function of probe (X_{probe}) and pump (X_{pump}) positions for V_G = 0 V and t_{delay} = 2 ps. (b) Three-dimensional spatiotemporal image, which is constructed by accumulating the two-dimensional images shown in (a) as a function of t_{delay} (from 0 to 100 ps). (c) Plots of ΔI_{pr} measured at positions S (blue line) and D (red line) as a function of t_{delay} when the pump pulse illuminates the center of the NW, as indicated by position B in (a). The black solid line indicates the results of the numerical calculation based on a transient diffusion model.

linearly with the pump power energy, far below the saturation regime (Supporting Information S5).

As previously mentioned, fs-SPCM is a powerful technique for investigating carrier dynamics for nanoscale systems with a very low cross section, such as thin NWs and SWNTs. The results for the SWNT ($\tau_{peak} \sim 5$ ps for 4 μm separation) and the Si NWs with a diameter of 30 nm ($\tau_{peak} \sim 16$ ps for 1 μm separation) are shown in the Supporting Information S6 and S7. In particular, the transit time of the SWNT device is about 10 times shorter than that of Si NWs with similar channel length because of the higher SWNT mobility. The transit time has not been measured before in SWNTs by using the spatially separated pump and probe pulses, whereas the previous optical and photocurrent microscope used the collinear pump and probe pulses.[17,18,29,30] On the other hand, the RF measurements revealed the cutoff frequency of less than ~15 GHz for an individual SWNT device and ~150 GHz for network SWNTs.[35−37] Our results simply imply that the intrinsic cutoff frequency of individual SWNT devices could reach 1 THz for $l_{ch} < 1$ μm.

Using the techniques presented in this paper, carrier dynamics based on a fixed pump position (located at the metallic contact region) have been successfully demonstrated by recording the value of I_{pr} as a function of the probe position. Here, we address carrier dynamics as a function of both the pump and the probe positions by introducing a novel technique based on pump−probe photocurrent correlation images. A representative image measured at V_G = 0 V and t_{delay} = 2 ps is shown in Figure 3a. X_{probe} and X_{pump} represent the positions of the probe and the pump spots, respectively, and therefore, the solid diagonal line indicates the region where the two pulses spatially overlap. This image is particularly useful for identifying pump locations where nanoscale devices experience interesting dynamical phenomena. A dramatic decrease in I_{pr} is clearly visible where there is a spatial overlap between the pump and the probe pulses at approximately zero delay. As expected, ΔI_{pr} is noticeable when the pump pulse is positioned near the metallic contacts (denoted by A and C).

A three-dimensional spatiotemporal image can be constructed by accumulating two-dimensional pump−probe correlation images as a function of t_{delay}. A series of correlation images are shown in Figure 3b as a function of t_{delay}, ranging from 0 to 100 ps, with a 20 ps interval. When the pump pulse illuminates a band-bending region around A or C, the dynamical behaviors of I_{pr} are consistent with the behaviors in Figure 2. In particular, we observe an abrupt decrease in I_{pr} at t_{delay} = 0 ps when the pump and probe pulses are spatially overlapped (diagonal positions) and a delayed change in I_{pr} at opposite electrodes, as indicated by red and blue arrows (off-diagonal positions).

Interestingly, we can also observe the dynamical change in I_{pr} when the pump pulse illuminates a flat-band region [*i.e.*, the middle of the NW (denoted by B in Figure 3a)], although they are overshadowed by the metallic signals. This phenomenon occurs when pump-induced carrier dynamics are dominated by the pure diffusion process because there is no built-in electric field. In Figure 3c, we show a plot of ΔI_{pr} measured at the metallic contacts (positions S and D) as a function of t_{delay} when X_{pump} is located at the center of the NW for the higher pump energy of 5 pJ/pulse. We found a gradual increase in ΔI_{pr} as a function of t_{delay}, which likely results from holes migrating through the diffusion process. The τ_{peak} value of ~200 ps is in good agreement with value generated by numerical calculation (represented by a black solid line) using the time-dependent carrier diffusion equation (Supporting Information S8).

It is crucial to address dynamical carrier movements in terms of various working conditions, such as the source-drain bias and the gate bias, which are configurations that strongly modify the electronic band structures of NWs. While it is easily expected that the external bias voltages will influence overall carrier velocity, they are also capable of manipulating the shape of ultrashort carrier pulses. We first address carrier dynamics with respect to source-drain bias voltage (V_{SD}) for a device with l_{ch} = 6.5 μm. We show in Figure 4a a line profile of I_{pr} without the pump pulse for the five different V_{SD} values from −100 to 100 mV. For the relatively low bias conditions, the potential drop is dominant near the metal contacts, as schematically shown in Figure 4b. We measured I_{pr} at the opposite electrode D as a function of t_{delay} for the fixed pump position at S. Figure 4c shows ΔI_{pr} as a function of t_{delay} with $V_G = 0$. At this gate bias condition (*i.e.*, near flat-band condition, as will be discussed later), ΔI_{pr} spreads over hundreds of picoseconds for V_{SD} = 0 (black line). For negative bias conditions ($V_{SD} < 0$), ΔI_{pr} extends even further in the time domain (red and pink lines); however, for positive biases ($V_{SD} > 0$), ΔI_{pr} decays rapidly, demonstrating a significant narrowing of the electrical pulse width (blue and green lines).

This is because, for $V_{SD} < 0$, the electrostatic potential is lower at the probe position (D) than that of the pump position (S) with respect to hole carriers. In other words, many carriers with the low kinetic energies can reach the opposite electrodes efficiently, and this leads to the significant spreads in the transit time. Conversely, for $V_{SD} > 0$, the potential at the opposite electrode is higher, and this reduces the number of the carriers that arrive at the opposite electrode. In other words, only carriers with the higher kinetic energies can reach the opposite electrode, resulting in the narrowing of the electrical pulse width. We also found similar behaviors on a thin NW device which demonstrates significant narrowing of the carrier pulse for $V_{SD} > 0$ (Supporting Information S7). In general, the temporal shape of the electrical pulse generated at the Schottky contacts by the femtosecond lasers broadens significantly while propagating in the NWs (also see Supporting Information S8). However, our results suggest a possibility of electrical pulse shaping though *velocity filtering*, controlled by the external electrodes. Therefore, it will be possible to improve the bandwidth of the high-speed devices by adding a local potential barrier in the middle of NWs.

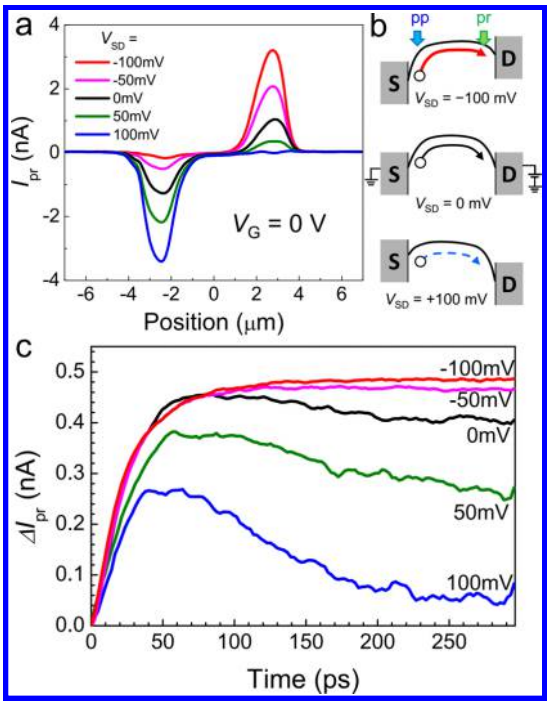

Figure 4. Source-drain bias voltage dependence. (a) Line profiles of I_{pr} along Si NW axis without pump pulse for a device with l_{ch} = 6.5 μm for five different V_{SD} values. PC spots are localized near metallic contacts regardless of V_{SD} for low bias conditions, whereas the strength of S and D signals varies with V_{SD}. (b) Schematic representation of the electrostatic potentials extracted from (a). (c) Plot of ΔI_{pr} as a function of time delay with the presence of pump pulse at position S for the five different V_{SD} values.

From now on, we focus on the gate-dependent dynamical behaviors of the photogenerated carriers. Figure 5a shows the dc conductivity of the device (l_{ch} = 4 μm) as a function of V_G. The high on-state current and the large transconductance for the n-type region mainly result from Si electron mobility, which is higher than the hole mobility.[38,39] Based on this plot, a band gap region is clearly defined and ranges from −12.2 to +11.5 V; we can thereby obtain a gate efficiency parameter α of 0.047.[40] Figure 5b shows a plot of ΔI_{pr} as a function of t_{delay} for the four different gate bias configurations. The transit time increases significantly as we increase V_G from −30 to 15 V. The time constants τ_c were obtained by fitting the time traces, and the results are plotted in Figure 5c. In particular, τ_c

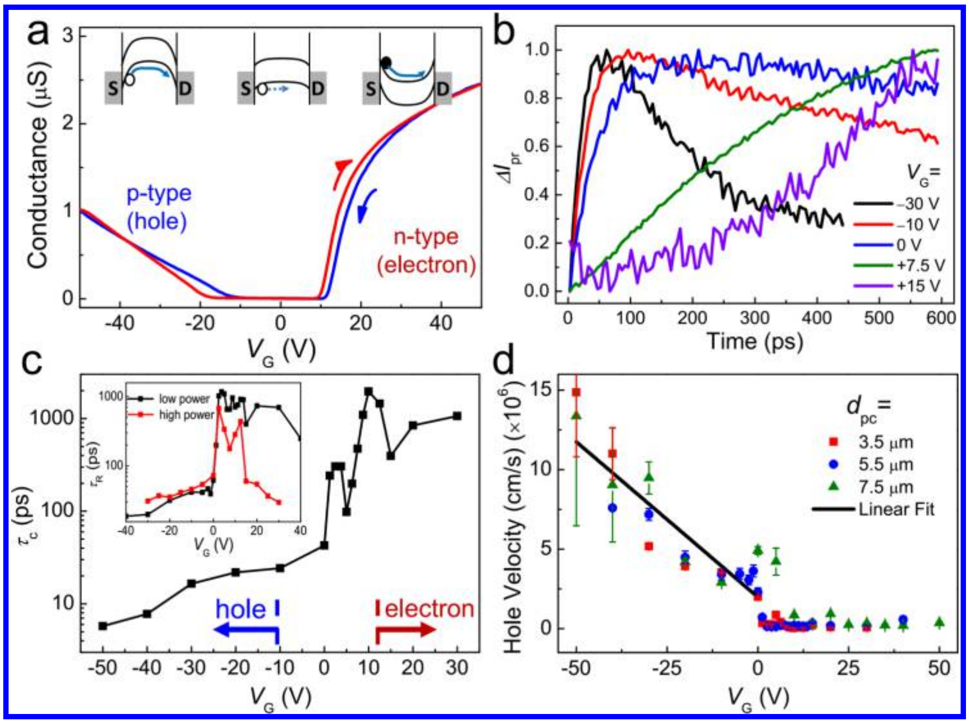

Figure 5. Gate-dependent carrier transport phenomena. (a) Direct current conductance as a function of V_G for the sample with $d_{pc} = 3.5$ μm with a relatively low pump intensity of $I_0 = 0.6$ pJ/pulse. (Insets) Schematic diagrams of the gate-dependent band alignments. Electric field strength in the depletion region decreases as V_G increases in p-type operation (from -50 to 0 V); consequently, initial speed of the injected carriers decreases accordingly. (b) Normalized time traces of ΔI_{pr} for various values of V_G. (c) τ_c as a function of V_G. τ_c increase from 6 ps ($V_G = -50$ V) to 43 ps ($V_G = 0$ V). (Inset) τ_c as a function of V_G with $d_{pc} = 5.5$ μm for both low- (I_0) and high-intensity (10 I_0) conditions. (d) v_{peak} as a function of V_G for the three devices with different values of d_{pc} (3.5, 5.5, and 7.5 μm). The solid line is a linear fit for the data with $V_G < 0$.

increases rapidly for $V_G > 0$ V, and this increase reflects the significant reduction in the band-bending strength in the NWs (*i.e.*, the suppressed drift motions). It is likely that carrier transport is dominated by a hole diffusion process for $V_G > 10$ V.

Because the band-bending direction is reversed for $V_G > 10$ V, the electron carriers (instead of the hole carriers) are injected toward the opposite electrode. Therefore, it is surprising that we cannot observe experimental evidence regarding electron transport phenomena in the n-type operating condition. This limitation likely occurs because we use a device with moderately n-doped materials; specifically, our technique is best suited for interrogating the dynamics of the minority carrier.[41] However, if we increase the pump intensity by a factor of 10 (as shown in the inset of Figure 5c), a dramatic reduction is observed for n-type operation (*e.g.*, $\tau_c \sim 30$ ps at $V_G = 30$ V for the sample with $d_{pc} \sim 5.5$ μm), and this finding likely results from the transport of electrons.

Corresponding to the maximum ΔI_{pr}, the most probable hole velocity (v_{peak}) in Figure 5b is plotted as a function of V_G, as shown in Figure 5d. For this plot, we use the gate-dependent transit times obtained from Figure 5c and the following relation $\tau_{peak} \approx 3.5\ \tau_c$. We combine the results for three devices with different channel lengths of 4, 6, and 8 μm (with d_{pc} of 3.5, 5.5, and 7.5 μm, respectively). The velocity decreases linearly as the field strength is reduced, and this result is in accordance with the change in the gate potential (from $V_G = -50$ V to $V_G = 0$ V). This finding is expected because of the field-dependent drift velocity of $\vec{v} = \mu_h \vec{E}$, where μ_h is the hole mobility and $\vec{E}$ represents the localized electric fields. Here it is reasonable assumption that the electric fields in the depletion layer is proportional to the applied gate bias voltage, which is confirmed by the band alignment measurements extracted from SPCM (see Supporting Information S5). By fitting the data and applying the gate efficiency parameter, we extracted a minority hole mobility of 200 cm^2/Vs, which is in reasonable agreement with the known value.[38,39]

It is interesting that the gate-dependent velocity measured at opposite electrodes does not change noticeably for different channel lengths. This finding is a significant deviation from simulation results with a transient drift-diffusion model, which predicts a drastic decrease in v_{peak} when l_{ch} is larger than the width of the depletion layer (500 nm) (Supporting Information S8). In general, the carrier velocity tends to decrease rapidly when carriers are subject to a pure diffusion process outside the depletion region. However, our experimental data suggest that the average carrier velocity is independent of l_{ch}. This finding is described as drift-like motion, which has been reported previously in time-of-flight measurements.[42] Attributed to both surface recombination effects and the unique transport properties at high carrier kinetic energies, this phenomenon necessitates future study using a kinetic model that includes non-equilibrium initial carrier distributions. In addition, these effects could possibly explain why the carrier velocity reaches as high as the saturation velocity of $\sim 10^7$ cm/s for the high gate bias conditions,[38] which is relatively large even if we consider possible errors that are linked to the electrical pulse broadening at the detection position.

CONCLUSION

In summary, we developed a novel technique based on ultrafast photocurrent microscopy by combining scanning photocurrent microscopy and ultrafast pump−probe techniques. The transport of carriers created by the femtosecond pump pulse has been imaged by observing the change in the probe photocurrent. In particular, we measured the transit time of the carriers transported to opposite electrodes. We studied carrier dynamics in various working conditions, such as source-drain and gate biases. Gate-dependent measurements reveal that the carrier velocity changes linearly with the applied gate bias in accordance with changes in the electric field strength in the Schottky barrier. Conversely, the source-drain bias control results in the tailoring of the ultrashort electrical pulses. We observed drift-like motion, in which the average velocity did not change noticeably with changes in the channel length (up to 8 μm). Based on these results, it will be possible to design novel devices in which we create ultrafast carrier pulses and simultaneously control their movements. This work represents an important step toward understanding ultrafast dynamics in various nanoscale devices and toward developing future high-speed electronic devices.

METHODS

Femtosecond Scanning Photocurrent Microscopy. A femtosecond Ti:sapphire laser (centered at 800 nm with a repetition rate of 80 MHz and a pulse width of 60 fs) is used to locally photoexcite a NW device. The laser beams were divided into pump and probe beams, and t_{delay} is generated by a delay stage, which is located in the path of the pump beam. A pair of chirped mirrors (CM) is used to compensate for the positive dispersion that originates mainly from the objective lens. The pump and probe pulses are focused on the samples using the objective lens (100× and NA 0.80), which has a full width at half-maximum of 600 nm. A pair of two-axis steering mirrors (Newport Corporation, Inc.) is used to manipulate the positions of both focused laser spots. An optical modulator (Boston Micromachines Corporation) is used to optically modulate the probe pulse at 20 kHz to capture only the I_{pr} signals and to exclude the photocurrents generated directly by the pump pulse. This modulator is advantageous over the acousto-optic types because it is free from the dispersion effects and delivers better spatial resolution for the focused laser. I_{pr} is measured using a high-speed current preamplifier (FEMTO Messtechnik GmbH) and a subsequent lock-in amplifier (Signal Recovery) operated at the probe modulation frequency. Each image was taken within 10 s, whereas the rest of the technical details for fast SPCM imaging can be found elsewhere.[27]

Device Fabrication. Si NW FETs shown in the main text are fabricated from silicon-on-insulator wafers (Soitec, Inc.), which have an oxide layer (1 μm) and a moderately doped n-type Si layer (thickness of 200 nm and doping concentration of 1.6×10^{16} cm^{-3}). NW patterns are generated with widths of 200−300 nm and channel lengths of 4−10 μm, by an electron-beam lithography technique followed by inductively coupled plasma etching.[43,44] Etched Si NWs are then electrically connected by Ni and Au (50 and 200 nm, respectively) electrodes using electron-beam lithography. After these processes, the device is annealed at 250 °C for 10 min under an Ar atmosphere. Scanning electron microscopy image of the device is shown in Supporting Information S1.

Conflict of Interest: The authors declare no competing financial interest.

Acknowledgment. This work was supported by Midcareer Researcher Programs (2011-0016173) and by PRC Program (2009-0094046) through National Research Foundation grant funded by the Korea Government.

Supporting Information Available: Supporting Information S1−S8. This material is available free of charge *via* the Internet at http://pubs.acs.org.

REFERENCES AND NOTES

1. Avouris, P.; Chen, Z.; Perebeinos, V. Carbon-Based Electronics. *Nat. Nanotechnol.* **2007**, *2*, 605–615.
2. Lieber, C. M.; Wang, Z. L. Functional Nanowires. *MRS Bull.* **2007**, *32*, 99–108.
3. Duan, X.; Fu, T. M.; Liu, J.; Lieber, C. M. Nanoelectronics-Biology Frontier: From Nanoscopic Probes for Action Potential Recording in Live Cells to Three-Dimensional Cyborg Tissues. *Nano Today* **2013**, *8*, 351–373.
4. Yan, R.; Gargas, D.; Yang, P. Nanowire Photonics. *Nat. Photonics* **2009**, *3*, 569–576.
5. Claudon, J.; Bleuse, J.; Malik, N. S.; Bazin, M.; Jaffrennou, P.; Gregersen, N.; Sauvan, C.; Lalanne, P.; Gérard, J. M. A Highly Efficient Single-Photon Source Based on a Quantum Dot in a Photonic Nanowire. *Nat. Photonics* **2010**, *4*, 174–177.
6. Grzela, G.; Paniagua-Domínguez, R.; Barten, T.; Fontana, Y.; Sánchez-Gil, J. A.; Gómez Rivas, J. Nanowire Antenna Emission. *Nano Lett.* **2012**, *12*, 5481–5486.
7. Benali, A.; Traversa, F. L.; Albareda, G.; Aghoutane, M.; Oriols, X. Improving the Intrinsic Cut-Off Frequency of Gate-All-Around Quantum-Wire Transistors without Channel Length Scaling. *Appl. Phys. Lett.* **2013**, *102*, 173506.
8. Friedman, R. S.; McAlpine, M. C.; Ricketts, D. S.; Ham, D.; Lieber, C. M. Nanotechnology: High-Speed Integrated Nanowire Circuits. *Nature* **2005**, *434*, 1085–1085.
9. Rutherglen, C.; Jain, D.; Burke, P. Nanotube Electronics for Radiofrequency Applications. *Nat. Nanotechnol.* **2009**, *4*, 811–819.
10. Kocabas, C.; Dunham, S.; Cao, Q.; Cimino, K.; Ho, X.; Kim, H. S.; Dawson, D.; Payne, J.; Stuenkel, M.; Zhang, H.; *et al.* High-Frequency Performance of Submicrometer Transistors That Use Aligned Arrays of Single-Walled Carbon Nanotubes. *Nano Lett.* **2009**, *9*, 1937–1943.
11. Xia, F.; Mueller, T.; Lin, Y. M.; Valdes-Garcia, A.; Avouris, P. Ultrafast Graphene Photodetector. *Nat. Nanotechnol.* **2009**, *4*, 839–843.
12. Schwierz, F. Graphene Transistors. *Nat. Nanotechnol.* **2010**, *5*, 487–496.
13. Shah, J. *Ultrafast Spectroscopy of Semiconductors and Semiconductor Nanostructures*; Springer: Berlin, 1999; Vol. 115.

14. Seo, M. A.; Yoo, J.; Dayeh, S. A.; Picraux, S. T.; Taylor, A. J.; Prasankumar, R. P. Mapping Carrier Diffusion in Single Silicon Core−Shell Nanowires with Ultrafast Optical Microscopy. *Nano Lett.* **2012**, *12*, 6334–6338.
15. Gabriel, M. M.; Kirschbrown, J. R.; Christesen, J. D.; Pinion, C. W.; Zigler, D. F.; Grumstrup, E. M.; Mehl, B. P.; Cating, E. E. M.; Cahoon, J. F.; Papanikolas, J. M. Direct Imaging of Free Carrier and Trap Carrier Motion in Silicon Nanowires by Spatially-Separated Femtosecond Pump−Probe Microscopy. *Nano Lett.* **2013**, *13*, 1336–1340.
16. Gabriel, M. M.; Grumstrup, E.; Kirschbrown, J. R.; Pinion, C. W.; Christesen, J. D.; Zigler, D. F.; Cating, E. M.; Cahoon, J. F.; Papanikolas, J. M. Imaging Charge Separation and Carrier Recombination in Nanowire p-i-n Junctions Using Ultrafast Microscopy. *Nano Lett.* **2014**, *14*, 3079–3087.
17. Gao, B.; Hartland, G. V.; Huang, L. Transient Absorption Spectroscopy and Imaging of Individual Chirality-Assigned Single-Walled Carbon Nanotubes. *ACS Nano* **2012**, *6*, 5083–5090.
18. Gao, B.; Hartland, G. V.; Huang, L. Transient Absorption Spectroscopy of Excitons in an Individual Suspended Metallic Carbon Nanotube. *J. Phys. Chem. Lett.* **2013**, *4*, 3050–3055.
19. Lo, S. S.; Shi, H. Y.; Huang, L.; Hartland, G. V. Imaging the Extent of Plasmon Excitation in Au Nanowires Using Pump−Probe Microscopy. *Opt. Lett.* **2013**, *38*, 1265–1267.
20. Cui, Q.; Ceballos, F.; Kumar, N.; Zhao, H. Transient Absorption Microscopy of Monolayer and Bulk WSe_2. *ACS Nano* **2014**, *8*, 2970–2976.
21. Ahn, Y. H.; Dunning, J.; Park, J. Scanning Photocurrent Imaging and Electronic Band Studies in Silicon Nanowire Field Effect Transistors. *Nano Lett.* **2005**, *5*, 1367–1370.
22. Gu, Y.; Kwak, E. S.; Lensch, J. L.; Allen, J. E.; Odom, T. W.; Lauhon, L. J. Near-Field Scanning Photocurrent Microscopy of a Nanowire Photodetector. *Appl. Phys. Lett.* **2005**, *87*, 043111.
23. Ahn, Y. H.; Tsen, A. W.; Kim, B.; Park, Y. W.; Park, J. Photocurrent Imaging of p-n Junctions in Ambipolar Carbon Nanotube Transistors. *Nano Lett.* **2007**, *7*, 3320–3323.
24. Graham, R.; Miller, C.; Oh, E.; Yu, D. Electric Field Dependent Photocurrent Decay Length in Single Lead Sulfide Nanowire Field Effect Transistors. *Nano Lett.* **2011**, *11*, 717–722.
25. Burghard, M.; Mews, A. High-Resolution Photocurrent Mapping of Carbon Nanostructures. *ACS Nano* **2012**, *6*, 5752–5756.
26. Wu, C. C.; Jariwala, D.; Sangwan, V. K.; Marks, T. J.; Hersam, M. C.; Lauhon, L. J. Elucidating the Photoresponse of Ultrathin MoS_2 Field-Effect Transistors by Scanning Photocurrent Microscopy. *J. Phys. Chem. Lett.* **2013**, *4*, 2508–2513.
27. Park, J. K.; Son, B. H.; Park, J. Y.; Lee, S.; Ahn, Y. H. High-Speed Scanning Photocurrent Imaging Techniques on Nanoscale Devices. *Curr. Appl. Phys.* **2013**, *13*, 2076–2081.
28. DeBorde, T.; Aspitarte, L.; Sharf, T.; Kevek, J. W.; Minot, E. D. Photothermoelectric Effect in Suspended Semiconducting Carbon Nanotubes. *ACS Nano* **2014**, *8*, 216–221.
29. Sun, D.; Aivazian, G.; Jones, A. M.; Ross, J. S.; Yao, W.; Cobden, D.; Xu, X. Ultrafast Hot-Carrier-Dominated Photocurrent in Graphene. *Nat. Nanotechnol.* **2012**, *7*, 114–118.
30. Gabor, N. M.; Zhong, Z.; Bosnick, K.; McEuen, P. L. Ultrafast Photocurrent Measurement of the Escape Time of Electrons and Holes from Carbon Nanotube p-i-n Photodiodes. *Phys. Rev. Lett.* **2012**, *108*, 087404.
31. Prechtel, L.; Song, L.; Schuh, D.; Ajayan, P.; Wegscheider, W.; Holleitner, A. W. Time-Resolved Ultrafast Photocurrents and Terahertz Generation in Freely Suspended Graphene. *Nat. Commun.* **2012**, *3*, 646.
32. Erhard, N.; Seifert, P.; Prechtel, L.; Hertenberger, S.; Karl, H.; Abstreiter, G.; Koblmüller, G.; Holleitner, A. W. Ultrafast Photocurrents and THz Generation in Single InAs-Nanowires. *Ann. Phys. (Berlin, Ger.)* **2012**, *525*, 180–188.
33. Park, J. K.; Kang, J. C.; Kim, S. Y.; Son, B. H.; Park, J. Y.; Lee, S.; Ahn, Y. H. Diffusion Length in Nanoporous Photoelectrodes of Dye-Sensitized Solar Cells under Operating Conditions Measured by Photocurrent Microscopy. *J. Phys. Chem. Lett.* **2012**, *3*, 3632–3638.
34. Park, J. D.; Son, B. H.; Park, J. K.; Kim, S. Y.; Park, J. Y.; Lee, S.; Ahn, Y. H. Diffusion Length in Nanoporous TiO_2 Films under Above-Band-Gap Illumination. *AIP Adv.* **2014**, *4*, 067106.
35. Wang, D.; Yu, Z.; McKernan, S.; Burke, P. J. Ultrahigh Frequency Carbon Nanotube Transistor Based on a Single Nanotube. *IEEE Trans. Nanotechnol.* **2007**, *6*, 400–403.
36. Rouhi, N.; Jain, D.; Burke, P. J. Nanoscale Devices for Large-Scale Applications. *IEEE Microwave Mag.* **2010**, *11*, 72–80.
37. Steiner, M.; Engel, M.; Lin, Y. M.; Wu, Y.; Jenkins, K.; Farmer, D. B.; Humes, J. J.; Yoder, N. L.; Seo, J. W. T.; Green, A. A.; *et al.* High-Frequency Performance of Scaled Carbon Nanotube Array Field-Effect Transistors. *Appl. Phys. Lett.* **2012**, *101*, 053123.
38. Canali, C.; Majni, G.; Minder, R.; Ottaviani, G. Electron and Hole Drift Velocity Measurements in Silicon and their Empirical Relation to Electric Field and Temperature. *IEEE Trans. Electron Devices* **1975**, *22*, 1045–1047.
39. Neugroschel, A. Minority-Carrier Diffusion Coefficients and Mobilities in Silicon. *IEEE Electron Device Lett.* **1985**, *6*, 425–427.
40. Rosenblatt, S.; Yaish, Y.; Park, J.; Gore, J.; Sazonova, V.; McEuen, P. L. High Performance Electrolyte Gated Carbon Nanotube Transistors. *Nano Lett.* **2002**, *2*, 869–872.
41. Streetman, B. G.; Banerjee, S. *Solid State Electronic Devices*, 6th ed.; Prentice Hall: Englewood Cliffs, NJ, 2005; Vol. 4.
42. Laurich, B.; Hillmer, H.; Forchel, A. Optical Time-of-Flight Investigation of the Exciton Transport in Silicon. *J. Appl. Phys.* **1987**, *61*, 1480–1485.
43. Park, I.; Li, Z.; Pisano, A. P.; Williams, R. S. Top-Down Fabricated Silicon Nanowire Sensors for Real-Time Chemical Detection. *Nanotechnology* **2009**, *21*, 015501.
44. Stern, E.; Klemic, J. F.; Routenberg, D. A.; Wyrembak, P. N.; Turner-Evans, D. B.; Hamilton, A. D.; LaVan, D. A.; Fahmy, T. M.; Reed, M. A. Label-Free Immunodetection with CMOS-Compatible Semiconducting Nanowires. *Nature* **2007**, *445*, 519–522.